

<https://doi.org/10.1038/s43246-025-00932-x>

# A complex hydride-based electrolyte additive for rechargeable Li–S batteries



Sojeong Kim<sup>1,9</sup>, Junyoung Heo<sup>2,3,9</sup>, Hawon Gu<sup>2,3</sup>, Huijeong Oh<sup>1</sup>, Taeyoung Lee<sup>1</sup>, Youngju Lee<sup>4</sup>, Kazuaki Kisu<sup>5,6</sup>, Shin-ichi Orimo<sup>6,7</sup>, Jun-Woo Park<sup>8,2,3</sup> & Sangryun Kim<sup>1,8</sup>✉

Lithium–sulfur (Li–S) batteries are considered promising next-generation energy storage systems due to their high energy density, low-cost S cathodes, and potential for sustainable large-scale applications. However, they face significant challenges, including the lithium polysulfides (LiPS) shuttle effect associated with the S cathodes and interfacial reactions at the Li metal anodes, which occur concurrently and hinder their stable operation. To address these simultaneous issues at both the cathode and anode, we propose the use of complex hydrides as an electrolyte additive. *C*-*oso*-type complex hydride  $\text{Li}(\text{CB}_{11}\text{H}_{12})$  dissociates in the electrolyte to form mobile lithium cations and rigid polyanionic complex anions  $[\text{CB}_{11}\text{H}_{12}]^-$ , which form  $\text{Li}^+$ –solvent coordination by its weak coordinating ability. The weakened solvation free energy and the reducing ability of this modified electrolyte suppress LiPS dissolution at the S cathode as well as facilitates stable lithium anode reaction, enhancing the cycling stability and coulombic efficiency of Li–S batteries. The findings of this study underscore the importance of designing electrolyte structures using various complex hydrides and highlight their potential to address the limitations of Li–S batteries, paving the way for future advancements in this field.

The demand for energy sources is continuously increasing<sup>1</sup>, driving the need for battery systems with higher energy density and longer cycle life than conventional lithium-ion batteries<sup>2</sup>. Li–S batteries have garnered significant attention as next-generation energy storage systems because they utilize high energy density S (theoretical capacity = 1672 mAh g<sup>−1</sup>)<sup>3–5</sup> cathodes and Li metal (theoretical capacity = 3860 mAh g<sup>−1</sup>, potential = −3.04 V vs. SHE)<sup>6</sup> anodes. This combination of high-energy density electrodes yields an exceptionally high theoretical energy density of over 2600 Wh kg<sup>−1</sup>. Moreover, S, employed as the cathode material, is abundant in the Earth's crust and environmentally benign, providing notable benefits in terms of cost-effectiveness and sustainability<sup>7–9</sup>.

Despite these advantages, several critical challenges must be addressed to enable the reliable operation of Li–S batteries. One major issue in Li–S batteries is the dissolution of LiPS and the accompanying parasitic reactions. During the discharge process, the conversion of sulfur to lithium sulfide proceeds via a solid–liquid–solid reaction mechanism<sup>10</sup>. This phase change

involves the generation of LiPS ( $\text{Li}_2\text{S}_x$ ,  $4 \leq x \leq 8$ ) as intermediates<sup>11</sup>, which dissolve into ether-based electrolytes and trigger the LiPS shuttle effect<sup>12,13</sup>. The shuttle effect of LiPS leads to the loss of active sulfur and undesirable interactions with the Li metal anodes, ultimately resulting in reduced coulombic efficiency and capacity fading. Furthermore, the Li metal anodes present additional limitations, such as dendrite formation and interfacial instability, both of which cause rapid cycling fading<sup>14–16</sup>. Since these simultaneous changes at the cathode and anode mutually accelerate each other, in most cases, the performance degradation of Li–S batteries is often more severe than that of conventional lithium-ion counterparts.

A number of approaches have been introduced to mitigate these challenges in Li–S batteries. Electrolyte additives have been one of the primary remedies, as the given interfacial phenomena at both the cathode and anode are strongly influenced by the structure of the electrolyte. A representative additive, lithium nitrate ( $\text{LiNO}_3$ ), forms a stable solid electrolyte interphase (SEI) on the Li metal anode surface, effectively

<sup>1</sup>Department of Chemistry, Gwangju Institute of Science and Technology (GIST), Gwangju, Republic of Korea. <sup>2</sup>Next Generation Battery Research Center, Korea Electrotechnology Research Institute (KERI), Changwon-si, Republic of Korea. <sup>3</sup>Department of Electro-Functionality Materials Engineering, University of Science and Technology (UST), Daejeon, Republic of Korea. <sup>4</sup>Honam Regional Center, Korea Basic Science Institute (KBSI), Gwangju, Republic of Korea. <sup>5</sup>College of Engineering, Shibaura Institute of Technology, Kotoku, Tokyo, Japan. <sup>6</sup>Institute for Materials Research (IMR), Tohoku University, Sendai, Japan. <sup>7</sup>WPI-Advanced Institute for Materials Research (WPI-AIMR), Tohoku University, Sendai, Japan. <sup>8</sup>Graduate School of Energy Convergence, Gwangju Institute of Science and Technology (GIST), Gwangju, Republic of Korea. <sup>9</sup>These authors contributed equally: Sojeong Kim, Junyoung Heo. ✉e-mail: [parkjw@keri.re.kr](mailto:parkjw@keri.re.kr); [sangryun@gist.ac.kr](mailto:sangryun@gist.ac.kr)

suppressing side reactions with LiPS<sup>17–19</sup>. Following this, other nitrate-based additives, such as CsNO<sub>3</sub><sup>20</sup>, KNO<sub>3</sub><sup>21</sup>, ZrO(NO<sub>3</sub>)<sub>2</sub><sup>22</sup>, LaNO<sub>3</sub><sup>23</sup>, and NaNO<sub>3</sub><sup>24</sup>, have been investigated. Additional additives, including SOCl<sub>2</sub> (forming LiCl-enriched SEI)<sup>25</sup>, KPF<sub>6</sub> (forming LiF-enriched SEI)<sup>26</sup>, and CuPc (containing copper sulfide)<sup>27</sup>, have also been developed to further improve the cycling performances. Despite significant progress, the development of additives for Li–S batteries remains limited by challenges such as complicated mechanistic interactions and long-term stability issues.

In this study, we propose a *closo*-type complex hydride, Li(CB<sub>11</sub>H<sub>12</sub>), as an additive for Li–S batteries. In ether-based electrolytes, Li(CB<sub>11</sub>H<sub>12</sub>) dissociates into Li<sup>+</sup> and disordered [CB<sub>11</sub>H<sub>12</sub>]<sup>−</sup> complex anions. The dissociated [CB<sub>11</sub>H<sub>12</sub>]<sup>−</sup> modifies the solvation structure around Li<sup>+</sup>, promoting Li<sup>+</sup>–solvent coordination while driving the anions outward. This modified electrolyte weakens LiPS solvation by reducing their solvation free energy, thereby suppressing the shuttle effect, while simultaneously forming a complex hydride-based interfacial layer that mitigates side reactions at the Li metal anodes.

Complex hydrides have been intensively investigated as solid-state electrolytes due to their high lithium-ion conductivity, low material density, and outstanding chemical/electrochemical stability against the Li metal anodes<sup>28–39</sup>. Based on these conspicuous properties, various types of all-solid-state batteries employing complex hydride solid electrolytes such as Li–S<sup>40–42</sup>, Li–TiS<sub>2</sub><sup>43,44</sup>, Li–LiCoO<sub>2</sub><sup>45</sup>, Li–NMC have been studied<sup>46,47</sup>. These characteristics of complex hydrides can be applied to a wide range of battery electrolyte systems, including aqueous and organic liquid electrolytes. Therefore, to the best of our knowledge, the utilization of complex hydrides as additives in liquid-electrolyte lithium batteries, such as those demonstrated in this study, represents an approach distinct from their conventional role in all-solid-state batteries.

## Results and discussion

### Electrolyte synthesis and solvation structure

Complex hydrides, generally denoted as M<sub>x</sub>(M'<sub>y</sub>H<sub>z</sub>), where M and M'<sub>y</sub>H<sub>z</sub> represent a metal cation and a complex anion, respectively, exhibit excellent chemical and electrochemical stability toward the Li metal anodes because of their strong reducing capability<sup>30,42</sup>. In particular, the *closo*-type complex hydride Li(CB<sub>11</sub>H<sub>12</sub>) includes a large cage-like [CB<sub>11</sub>H<sub>12</sub>]<sup>−</sup> polyatomic complex anion formed by strong covalent bonds among the central atoms (boron (B) and carbon (C)) and multiple hydrogen (H) atoms (Fig. 1a). The structure of the [CB<sub>11</sub>H<sub>12</sub>]<sup>−</sup> complex anion is characterized by delocalized electron-deficient bonding, which leads to weak electrostatic interactions with lithium-ions<sup>48,49</sup>. The X-ray diffraction (XRD) profile of Li(CB<sub>11</sub>H<sub>12</sub>) that is used as an electrolyte additive in this study is indexed by the orthorhombic unit cell, which is consistent with that of its low-temperature phase (space group Pca2<sub>1</sub> (Z = 4))<sup>32</sup> (Supplementary Fig. 1).

The electrolytes were prepared by simply mixing LiTFSI salt, LiNO<sub>3</sub> additive, DOL:DME solvent, and Li(CB<sub>11</sub>H<sub>12</sub>) additive. From the testing of various contents of Li(CB<sub>11</sub>H<sub>12</sub>) (Supplementary Fig. 2), 0.05 M was chosen as the main modified electrolyte in this investigation. Hereafter, the electrolytes prepared without and with 0.05 M Li(CB<sub>11</sub>H<sub>12</sub>) are denoted as pristine and 0.05 M Li(CB<sub>11</sub>H<sub>12</sub>), respectively. Figure 1b illustrates a schematic representation of Li<sup>+</sup> solvation structures in the pristine and 0.05 M Li(CB<sub>11</sub>H<sub>12</sub>) electrolytes. The Li(CB<sub>11</sub>H<sub>12</sub>) additive increases the number of solvent molecules surrounding Li<sup>+</sup> compared to the pristine electrolyte, as clarified by the subsequent Raman and nuclear magnetic resonance (NMR) analyses.

Vibrating modes of the constituent ions and molecules in the pristine and 0.05 M electrolytes were examined by Raman spectroscopy measurements (Fig. 1c and Supplementary Fig. 5). In the range of 700–800 cm<sup>−1</sup>, the Raman profile of the pristine electrolyte exhibits various CF<sub>3</sub> bending and S–N stretching modes of the TFSI<sup>−</sup> anion, including free TFSI<sup>−</sup> (solvent-separated ion pairs) at 739 cm<sup>−1</sup>, contact ion pairs (CIP; a TFSI<sup>−</sup> anion interacting with one Li<sup>+</sup>) at 744 cm<sup>−1</sup>, and aggregates (AGG; a TFSI<sup>−</sup> anion interacting with two or more Li<sup>+</sup> ions) at 749 cm<sup>−1</sup>, respectively<sup>50,51</sup>. For the 0.05 M Li(CB<sub>11</sub>H<sub>12</sub>) electrolyte, the peak intensity of free TFSI<sup>−</sup> increases,

whereas those of CIP and AGG decrease, indicating that the Li(CB<sub>11</sub>H<sub>12</sub>) additive reduces the involvement of TFSI<sup>−</sup> in Li<sup>+</sup>–anion pairing. In addition, the Raman spectra of the 830–890 cm<sup>−1</sup> and 1000–1060 cm<sup>−1</sup> regions of the pristine electrolyte present the Raman peaks from the DOL:DME solvents at 870 cm<sup>−1</sup> and 1024 cm<sup>−1</sup>, both of which correspond to Li<sup>+</sup>–coordinated solvent<sup>52</sup>. The intensity of the Li<sup>+</sup>–coordinated solvent peak is enhanced in the 0.05 M Li(CB<sub>11</sub>H<sub>12</sub>) electrolyte, which indicates strengthened Li<sup>+</sup>–solvent coordination. A similar weak interaction between Li<sup>+</sup> and anions was observed from the NO stretching modes of NO<sub>3</sub><sup>−</sup> anions. The Raman peaks at 1037, 1042, and 1052 cm<sup>−1</sup> represent free NO<sub>3</sub><sup>−</sup>, CIP (one Li<sup>+</sup> interacting with NO<sub>3</sub><sup>−</sup>), and AGG (NO<sub>3</sub><sup>−</sup> interacting with multiple Li<sup>+</sup>), respectively<sup>53</sup>. In the 0.05 M Li(CB<sub>11</sub>H<sub>12</sub>) electrolyte, the intensity of the free NO<sub>3</sub><sup>−</sup> peak increases, whereas that of the CIP and AGG peaks decreases compared to the pristine electrolyte, confirming a higher portion of NO<sub>3</sub><sup>−</sup> remaining in the free-ion state. Also, the enhanced peak at 1024 cm<sup>−1</sup> in the 0.05 M Li(CB<sub>11</sub>H<sub>12</sub>) electrolyte supports this interpretation, indicating enhanced Li<sup>+</sup>–solvent coordination.

These changes in the Li<sup>+</sup> solvation structure are accompanied by a significant modification in the symmetric structure of the [CB<sub>11</sub>H<sub>12</sub>]<sup>−</sup> complex anions, compared to that in solid-state Li(CB<sub>11</sub>H<sub>12</sub>). Solid-state Li(CB<sub>11</sub>H<sub>12</sub>) features multiple B–H stretching modes associated with anisotropic bonding, characterized by variations in their covalent bond lengths<sup>49,54</sup>, as reflected in its Raman profile that exhibits multiple B–H peaks. In contrast, in the 0.05 M Li(CB<sub>11</sub>H<sub>12</sub>) electrolyte, these modes are consolidated into two peaks, which imply that the B–H bonds become isotropic. The equalized bond lengths demonstrate a decrease in the symmetry of the [CB<sub>11</sub>H<sub>12</sub>]<sup>−</sup> complex anions (and thus an increase in disorder), as observed in the high-temperature phases of complex hydrides<sup>32,55</sup> of solid state Li(CB<sub>11</sub>H<sub>12</sub>). In the same context, the shift toward a higher Raman shift of the C–H stretching mode in the 0.05 M Li(CB<sub>11</sub>H<sub>12</sub>) electrolyte indicates a decrease in bond length, which can also be interpreted as a result of bond alignment in the [CB<sub>11</sub>H<sub>12</sub>]<sup>−</sup> complex anions. The <sup>7</sup>Li NMR spectrum of the 0.05 M Li(CB<sub>11</sub>H<sub>12</sub>) electrolyte exhibits a reduced chemical shift caused by the elevated electron density around Li<sup>+</sup>, reconfirming enhanced coordination by solvent molecules (Fig. 1d). The <sup>17</sup>O NMR peaks of the solvents also show a reduced chemical shift, which can be attributed to an increased coordination number around Li<sup>+</sup> that lowers the electron donation from each individual solvent molecule<sup>56,57</sup>. Moreover, the weakly coordinating anion [CB<sub>11</sub>H<sub>12</sub>]<sup>−</sup><sup>48,49</sup>, with its high reducing ability, preferentially interacts with solvent molecules, thereby enhancing the shielding of oxygen nuclei<sup>58,59</sup>. Consistently, the <sup>19</sup>F NMR spectrum of the 0.05 M Li(CB<sub>11</sub>H<sub>12</sub>) electrolyte shows a reduced chemical shift, indicating weakened Li<sup>+</sup>–TFSI<sup>−</sup> coordination. The increased Li diffusivity and the lowered H diffusivity also support the dominant interaction between Li<sup>+</sup> and solvent (Supplementary Fig. 3)<sup>60,61</sup>.

Overall, these findings reveal that the Li(CB<sub>11</sub>H<sub>12</sub>) additive forms a unique solvation structure in which solvent-solvated Li<sup>+</sup> ions and free anions coexist. This structural change can be understood by the low coordinating nature of the [CB<sub>11</sub>H<sub>12</sub>]<sup>−</sup> complex anions. It is well known that the disordering of complex anions in the solid-state complex hydrides significantly reduces interactions with surrounding ions<sup>42,62</sup>. Therefore, the disordered structure of the [CB<sub>11</sub>H<sub>12</sub>]<sup>−</sup> complex anions in the 0.05 M Li(CB<sub>11</sub>H<sub>12</sub>) electrolyte, as demonstrated by Raman analyses, directly reflects its weak coordinating ability. The redshift of the Raman peak associated with the symmetric vibrational mode of the *closo*-type anion in the 0.05 M Li(CB<sub>11</sub>H<sub>12</sub>) electrolyte (Supplementary Fig. 4) indicates weakened electrostatic interaction with Li<sup>+</sup>, supporting its role as a weakly coordinating anion. The weak coordinating characteristic of disordered [CB<sub>11</sub>H<sub>12</sub>]<sup>−</sup> complex anions weakens the interaction with anions such as TFSI<sup>−</sup> and NO<sub>3</sub><sup>−</sup>, thereby stabilizing primarily Li<sup>+</sup>–solvent coordination in the first solvation shell (Fig. 1b). This solvent-dominant solvation structure can suppress the stabilization and dissolution of LiPS, thereby potentially suppressing their solubility in the electrolyte. Importantly, as Li(CB<sub>11</sub>H<sub>12</sub>) contains multiple H atoms in its structure, even a small amount of this additive can effectively reconfigure the local solvation environment around Li<sup>+</sup>, potentially improving various aspects of the performance of Li–S

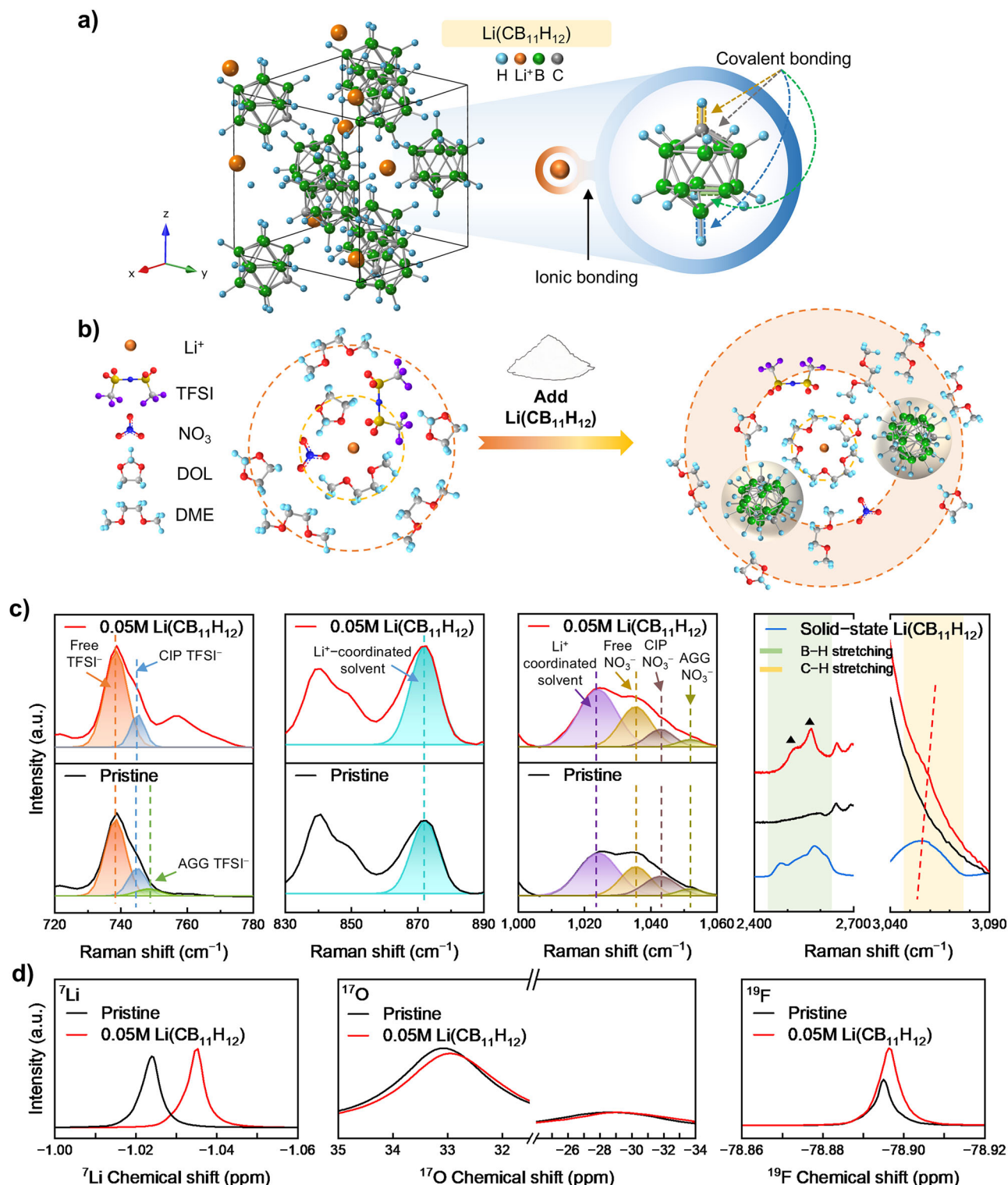


**Fig. 1 | Synthesis and characterization of the electrolyte. a** Crystal structure of  $\text{Li}(\text{CB}_{11}\text{H}_{12})$ , showing ionic bonding between  $\text{Li}^+$  and  $[\text{CB}_{11}\text{H}_{12}]^-$  and covalent bonding within the  $[\text{CB}_{11}\text{H}_{12}]^-$  complex anion. **b** Schematic illustration of the  $\text{Li}^+$  solvation structure in the pristine electrolyte and 0.05 M  $\text{Li}(\text{CB}_{11}\text{H}_{12})$  electrolyte. **c** Raman spectra of the pristine and 0.05 M  $\text{Li}(\text{CB}_{11}\text{H}_{12})$  electrolytes. **d** NMR (left:  $^7\text{Li}$ , middle:  $^{17}\text{O}$ , and right:  $^{19}\text{F}$ ) spectra of the pristine electrolyte and 0.05 M  $\text{Li}(\text{CB}_{11}\text{H}_{12})$  electrolytes.

batteries, as verified by the electrochemical characterization in the following section.

### Electrochemical properties

The electrochemical performance of both electrolytes was evaluated using Li–S cells. Detailed cell preparation and measurement conditions are

described in the Methods section. The 0.05 M  $\text{Li}(\text{CB}_{11}\text{H}_{12})$  electrolyte exhibited good electrochemical performance in various aspects, such as specific capacity, rate capability, and cycle life. Figure 2a shows the first discharge–charge profiles of cells with the 0.05 M  $\text{Li}(\text{CB}_{11}\text{H}_{12})$  electrolyte and pristine electrolyte under a current density of 0.1 C (1 C = 935.2 mAh  $\text{g}^{-1}$ ). When galvanostatically tested in the voltage range of

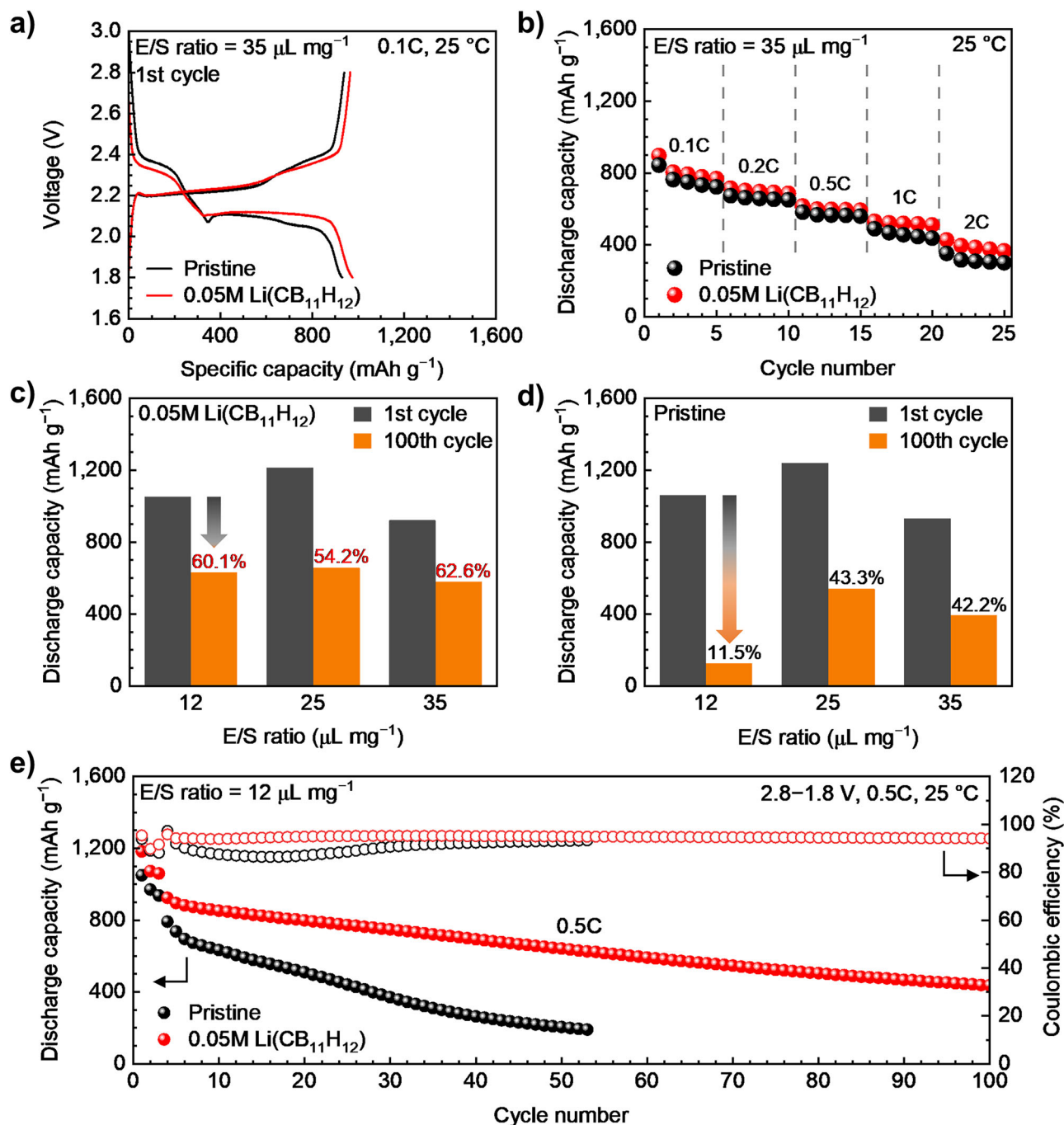


**Fig. 2 | Electrochemical performance of Li–S full cells. a** First discharge–charge voltage profiles of the pristine electrolyte and 0.05 M Li(CB<sub>11</sub>H<sub>12</sub>) electrolyte cells at 0.1 C. **b** Rate performance of the pristine electrolyte and 0.05 M Li(CB<sub>11</sub>H<sub>12</sub>) electrolyte cells at various C-rates. The E/S ratio was 35 μL mg<sup>-1</sup>. Discharge capacities after 1st and 100th cycles of **c** the pristine electrolyte and **d** 0.05 M Li(CB<sub>11</sub>H<sub>12</sub>)

electrolyte cells at various E/S ratios (12, 25, and 35 μL mg<sup>-1</sup>). The capacity retention between the 1st and 100th cycles was described as a percentage. **e** Cycling performances of discharge capacity and coulombic efficiency of the pristine electrolyte and 0.05 M Li(CB<sub>11</sub>H<sub>12</sub>) electrolyte cells at 0.5 C. The E/S ratio was 12 μL mg<sup>-1</sup>.

1.8–2.8 V vs. Li<sup>+</sup>/Li at 0.1 C, the 0.05 M Li(CB<sub>11</sub>H<sub>12</sub>) electrolyte cell presented higher first discharge and charge capacities than the pristine electrolyte. In the first discharge, the 0.05 M Li(CB<sub>11</sub>H<sub>12</sub>) electrolyte and pristine electrolyte cells delivered 895.9 and 843.1 mAh g<sup>-1</sup>, respectively, whereas in the first charge, they showed 896.7 and 852.9 mAh g<sup>-1</sup>, respectively.

The 0.05 M Li(CB<sub>11</sub>H<sub>12</sub>) cell also displayed improved rate capability (Fig. 2b and Supplementary Fig. 2). As the C-rate increased to 2, 5, 10, and 20 times from 0.1 C, the 0.05 M Li(CB<sub>11</sub>H<sub>12</sub>) cell retained 79.8%, 68.7%, 59.2%, and 47.6% of the capacity (895.9 mAh g<sup>-1</sup>) in the first cycle. In contrast, with

the same C-rate variations, the pristine electrolyte cell retained 79.8%, 68.8%, 57.9%, and 41.7%, even though its capacity (843.1 mAh g<sup>-1</sup>) in the first cycle was lower.

The enhanced cycling stability of the 0.05 M electrolyte cell was more pronounced under low E/S conditions (Fig. 2c, d, and Supplementary Figs. 6–8). The 0.05 M Li(CB<sub>11</sub>H<sub>12</sub>) electrolyte cells showed superior cycling stability during 100 cycles under all E/S ratios (12, 25, and 35 μL mg<sup>-1</sup>) used (Fig. 2c). Indeed, the capacity retention (60.1%) after 100 cycles at 12 μL mg<sup>-1</sup> was almost the same as that (62.6%) at 35 μL mg<sup>-1</sup>. The



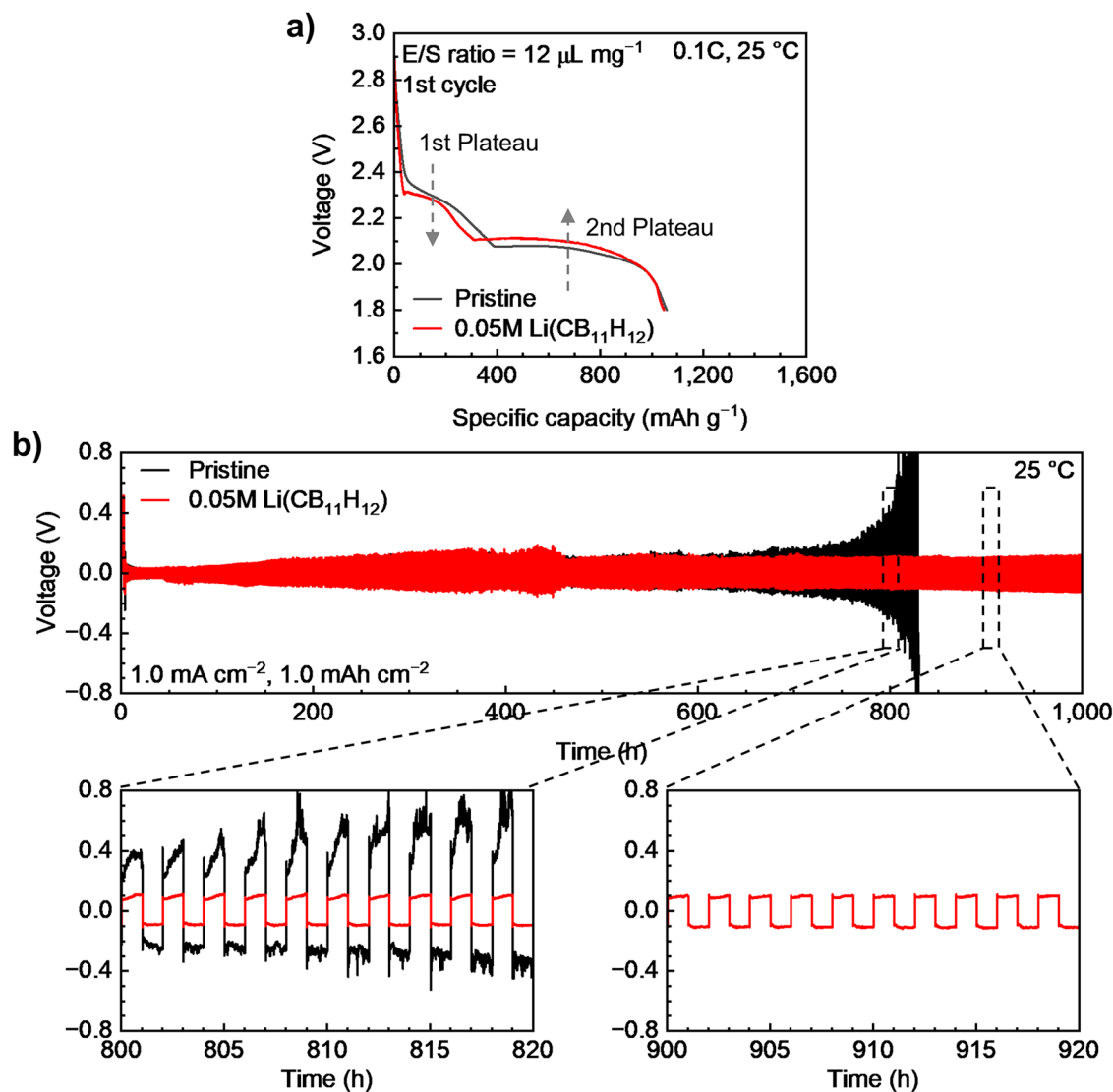


**Fig. 3 | Electrochemical reactions at the S cathodes and the Li metal anodes. a** First discharge voltage profiles of cells with the pristine electrolyte and 0.05 M Li(CB<sub>11</sub>H<sub>12</sub>) electrolyte at 0.1 C. **b** Galvanostatic cycling profiles of Li||Li symmetric cells at a current density of 1 mA cm<sup>-2</sup>. The areal capacity was 1 mAh cm<sup>-2</sup>.

discharge capacity after 100 cycles of the 0.05 M Li(CB<sub>11</sub>H<sub>12</sub>) electrolyte cell at 12  $\mu\text{L mg}^{-1}$  was 628.5 mAh g<sup>-1</sup> (Supplementary Fig. 8). However, the pristine electrolyte cell at 12  $\mu\text{L mg}^{-1}$  retained only 11.5% after 100 cycles. The enhanced cycling stability of the 0.05 M electrolyte was also reflected in the dQ/dV results (Supplementary Fig. 9). When measured at higher rates of 0.5 C, 1 C, and 2 C (after an initial 3 activation cycles at 0.05 C), the 0.05 M Li(CB<sub>11</sub>H<sub>12</sub>) electrolyte cell showed superior cycle retention compared to the pristine electrolyte counterpart (Fig. 2e and Supplementary Fig. 10). Moreover, under high sulfur loading (4 mg cm<sup>-2</sup>), the 0.05 M Li(CB<sub>11</sub>H<sub>12</sub>) electrolyte exhibited more stable cycling performance than the pristine electrolyte (Supplementary Fig. 11). The beneficial effect of the Li(CB<sub>11</sub>H<sub>12</sub>) additive was observed even in the absence of LiNO<sub>3</sub> (Supplementary Figs. 12 and 13).

The Li(CB<sub>11</sub>H<sub>12</sub>) additive resulted in improvements in kinetic behavior and stability. Based on these results, the electrochemical evaluation was expanded to measurements intended to separately assess the reactions of the S cathodes and the Li metal anodes. First, the potential difference method was employed to examine the relationship between LiPS dissolution from the S cathodes and the solvation structure of the electrolyte prepared. Figure 3a shows the discharge voltage profiles of the pristine electrolyte and 0.05 M Li(CB<sub>11</sub>H<sub>12</sub>) electrolyte cells during the first cycle at a current density of 0.1 C and an E/S ratio of 12  $\mu\text{L mg}^{-1}$ . Both cells exhibit two distinct

voltage plateaus; the 0.05 M Li(CB<sub>11</sub>H<sub>12</sub>) electrolyte cell displays a lower first plateau voltage ( $V_{1st}$ ) and a higher second plateau voltage ( $V_{2nd}$ ) compared to the pristine electrolyte counterpart.

In Li–S batteries, the discharge process proceeds through a two-step consecutive reaction, and because both the reactants (S, Li) and the final product (Li<sub>2</sub>S) are solid-phase species<sup>10,12</sup>, the overall Gibbs free energy change ( $\Delta G_{total}$ ) remains constant regardless of the electrolyte composition.  $V_{1st}$  observed originates from the formation of LiPS as an intermediate phase during the discharge reaction  $\text{Li}_{(s)} + \text{S}_{(s)} \leftrightarrow \text{LiPS}_{(sol)}$ , and thus this value is determined by the solvation free energy ( $\Delta G_{1, sol}$ ) of the generated LiPS. According to the relevant equation,  $\Delta G_{1, sol} = -nFV_{1st}$ , where  $n$  and  $F$  represent the number of moles of electrons and Faraday's constant, respectively, a weak solvation free energy during discharge results in a low  $V_{1st}$  (Supplementary Fig. 14)<sup>64,65</sup>. The high  $V_{2nd}$  detected can also be understood in the same context. Since the discharge process proceeds through a sequential two-step reaction, the overall free energy change ( $\Delta G_{total}$ ) remains constant. Thus, a decrease in  $\Delta G_{1, sol}$  leads to a corresponding increase in  $\Delta G_2$ .

Our structural analyses revealed that the Li(CB<sub>11</sub>H<sub>12</sub>) additive induces primary interactions between Li<sup>+</sup> and solvent molecules. Additionally, the [CB<sub>11</sub>H<sub>12</sub>]<sup>-</sup> complex anions exhibited a disordered state with very low coordination ability. It is therefore concluded that the decreased  $V_{1st}$  and the

increased  $V_{2nd}$  result from the reduced  $\Delta G_{l, sol}$  due to the  $\text{Li}(\text{CB}_{11}\text{H}_{12})$  additive. Moreover, this behavior can be applied to interpret the solubility of LiPS, as the  $\Delta G_{l, sol}$  is proportional to  $-\ln(K_{sp})$ , the solubility product constant<sup>64</sup>. Consequently, the lowered solvation free energy implies a reduced solubility of LiPS during cycling.

The solubility of LiPS was further examined experimentally using ultraviolet-visible (UV-vis) absorption spectroscopy (Supplementary Fig. 15). The  $\text{Li}_2\text{S}_6$  solution without any added electrolyte (referred to as the blank) exhibits characteristic absorption peaks of  $\text{S}_6^{2-}$  (470 nm) and  $\text{S}_4^{2-}$  (420 nm) species. After 12 h, the 0.05 M  $\text{Li}(\text{CB}_{11}\text{H}_{12})$  electrolyte exhibits lower absorbance peaks of  $\text{S}_6^{2-}$  and  $\text{S}_4^{2-}$  compared to the pristine counterpart, supporting that the  $\text{Li}(\text{CB}_{11}\text{H}_{12})$  additive effectively reduces the solubility of LiPS. Free solvent molecules are known to promote the formation of lithium polysulfides (LiPS)<sup>64,66,67</sup>. In contrast, our solvation structure analysis reveals that  $\text{Li}(\text{CB}_{11}\text{H}_{12})$  induces enhanced  $\text{Li}^+$ -solvent coordination. Consequently, the 0.05 M  $\text{Li}(\text{CB}_{11}\text{H}_{12})$  electrolyte mitigates the effect of free solvent molecules, leading to a reduced LiPS solubility.

Next, Li plating/stripping experiments were carried out to assess lithium-ion transfer capability across the Li metal anode interface. When galvanostatically cycled at a current density of  $1 \text{ mA cm}^{-2}$  with a constant capacity of  $1.0 \text{ mAh cm}^{-2}$ , the 0.05 M  $\text{Li}(\text{CB}_{11}\text{H}_{12})$  electrolyte cell exhibited superior cycle performance during 1000 h (Fig. 3b). In contrast, the pristine electrolyte cell indicates large voltage fluctuations, confirming unstable interfacial reactions. The slightly elevated overpotential observed during the initial cycles in the 0.05 M  $\text{Li}(\text{CB}_{11}\text{H}_{12})$  electrolyte is attributed to the high interfacial resistance prior to cell saturation (Supplementary Fig. 16). The stable Li plating/stripping reactions induced by the  $\text{Li}(\text{CB}_{11}\text{H}_{12})$  additive were also confirmed through measurements at various current densities (Supplementary Figs. 17 and 18), SEM analyses after cycling (Supplementary Fig. 19), and evaluations in  $\text{Li}||\text{Cu}$  cells (Supplementary Fig. 20). The enhanced stability against the Li metal anodes is ascribed to the reversible reaction by the strong reducing ability<sup>35,68</sup> of the  $\text{Li}(\text{CB}_{11}\text{H}_{12})$  additive.

### Analysis of the electrode interface and morphology

The electrochemical processes of the 0.05 M  $\text{Li}(\text{CB}_{11}\text{H}_{12})$  electrolyte cell were further investigated by various analyses. The SEM and XPS analyses on the S cathodes after 10 cycles present no significant changes in morphology and chemical state (Supplementary Figs. 21 and 22). These results indicate that the  $\text{Li}(\text{CB}_{11}\text{H}_{12})$  additive mainly affects the dissolution of LiPS identified in the potential difference analyses (Fig. 3a).

Therefore, our additional characterizations focus on the reaction of the lithium metal anodes. After cycling with the 0.05 M  $\text{Li}(\text{CB}_{11}\text{H}_{12})$  electrolyte at  $0.1 \text{ C}$ , SEM measurements reveal that the Li metal surface remains highly smooth and uniform (Fig. 4a). In contrast, the pristine electrolyte cells exhibit a rough and porous Li metal surface, which becomes progressively more damaged with ongoing cycles, likely due to continuous side reactions with the electrolyte (Fig. 4b).

To further investigate the reactions at the Li metal interfaces, XPS analyses were conducted. Importantly, the  $\text{S } 2p$  spectra indicate that in the 0.05 M  $\text{Li}(\text{CB}_{11}\text{H}_{12})$  electrolyte cell, the formation of the highly oxidized  $\text{Li}_x\text{SO}_y$  species is suppressed (Fig. 4c). It is known that the  $\text{Li}_x\text{SO}_y$  species are formed from the oxidation of LiPS and/or their side reactions with decomposition byproducts of  $\text{TFSI}^-$  and  $\text{NO}_3^-$  in the electrolyte<sup>17,69</sup>. In addition, the 0.05 M  $\text{Li}(\text{CB}_{11}\text{H}_{12})$  electrolyte cell exhibits a significantly higher ratio of LiPS among the surface compounds compared to the pristine cell, clarifying that their oxidation reactions are mitigated. Importantly, for the Li  $1s$  spectrum, a strong new peak, which is assigned to the complex hydride-based layer on the Li metal surface<sup>70</sup>, is observed at  $57 \text{ eV}$  in the 0.05 M  $\text{Li}(\text{CB}_{11}\text{H}_{12})$  electrolyte cell (Fig. 4d). These results suggest that the  $\text{Li}(\text{CB}_{11}\text{H}_{12})$  additive not only suppresses the dissolution of LiPS from the S cathode but also inhibits their subsequent oxidation at the lithium metal interface. The F  $1s$  and C  $1s$  spectra further confirm that the  $\text{Li}(\text{CB}_{11}\text{H}_{12})$  additive mitigates the formation of electrolyte decomposition byproducts, including  $\text{LiF}$ ,  $\text{CF}_3$ ,  $\text{ROLi}$ ,  $\text{HCO}_2\text{Li}$ ,  $\text{ROCO}_2\text{Li}$ , and  $\text{RCH}_2\text{OCO}_2\text{Li}$  (Fig. 4e, f)<sup>71,72</sup>. Our Li plating/stripping experiments (Fig. 3b) and SEM analyses

(Supplementary Fig. 19) demonstrated that the intrinsic reducing ability of  $\text{Li}(\text{CB}_{11}\text{H}_{12})$  additive stabilizes the interfacial reactions of the lithium metal anode, independently of its reactions with LiPS (Fig. 3b, Supplementary Figs. 17 and 18). In addition, the relative atomic concentrations of surface elements were quantitatively determined based on XPS survey scans (Supplementary Fig. 23 and Supplementary Table 1).

Therefore, the improved performances of the Li-S batteries are attributed to the synergistic effects of suppressed LiPS dissolution, mitigated LiPS oxidation, and stabilized Li metal plating/stripping reactions. The roles of the  $\text{Li}(\text{CB}_{11}\text{H}_{12})$  additive are graphically summarized in Fig. 4g.

To the best of our knowledge, this study represents the first application of a complex hydride additive in Li-S batteries, providing an important starting point for the further development of this material system. Our results offer a strategy for modulating the  $\text{Li}^+$  coordination environment and suggest the potential of a complex hydride additive to address fundamental limitations of the Li-S batteries. Together with the extensive research on Li-S batteries, prior studies have explored various additive chemistries<sup>23,73–75</sup>. In particular, ionic liquid-based additives designed to improve long-term cycling performance have shown substantial improvements through continuous developments of early-stage formulations<sup>76–80</sup>. In this work, although only  $\text{Li}(\text{CB}_{11}\text{H}_{12})$  was studied among various complex hydride candidates, it highlights the possibility of designing a broader range of complex hydride additives (e.g., other complex hydrides and mixed complex hydrides)<sup>42,43,55</sup>, which can enable diverse molecular and structural design.

## Conclusions

By adopting the *closo*-type complex hydride  $\text{Li}(\text{CB}_{11}\text{H}_{12})$  as an electrolyte additive, we have effectively enhanced the performance of Li-S batteries. In the Li-S battery liquid electrolyte, the  $[\text{CB}_{11}\text{H}_{12}]^-$  complex anions exhibit a weakly coordinating disordered state that induces enhanced interaction between  $\text{Li}^+$  and solvent molecules, thereby suppressing LiPS dissolution and mitigating the shuttle effect. Additionally, the  $\text{Li}(\text{CB}_{11}\text{H}_{12})$  additive forms a highly reducing complex hydride-based interfacial layer on the lithium metal anode, which not only reduces parasitic oxidation reactions of LiPS and electrolyte decompositions but also stabilizes the lithium metal interface. From a broader perspective, the insights provided in this work could be applied to a variety of liquid electrolyte systems that require weakly coordinating solvation structures and/or reducing environments.

## Methods

### Preparation of CNT-based S cathodes

Sulfur powder (Sigma Aldrich, 99.98%) and multi-walled carbon nanotubes (MWCNTs, Nanocyl, diameter =  $9.5 \text{ nm}$ ) were mixed in ethanol at a weight ratio of  $\text{S}:\text{MWCNT} = 7:3 \text{ wt.}\%$  using ball milling ( $450 \text{ rpm}$ ,  $30 \text{ min}$ ,  $10$  cycles) to ensure uniform dispersion. Ethanol was subsequently removed through vacuum filtration, and the obtained  $\text{MWCNT@S}$  mixture was dried in a vacuum oven at  $60^\circ\text{C}$  for  $12 \text{ h}$  to eliminate residual solvents. The dried mixture was then heated at  $155^\circ\text{C}$  for  $2 \text{ h}$  to facilitate the melt-diffusion of sulfur into the CNT network. The resulting  $\text{MWCNT@S}$  material was combined with Super P carbon black (SPB, Alfa Aesar) and carboxymethyl cellulose/styrene-butadiene rubber (CMC/SBR) in a weight ratio of  $8:1:1$ . The slurry was cast on an Al current collector using the doctor blade technique and dried in a vacuum oven at  $60^\circ\text{C}$  for  $12 \text{ h}$ . The loading density of final CNT-based sulfur cathodes was  $\sim 1.3 \text{ mg cm}^{-2}$ .

### Preparation of carbon-coated separator

The carbon mixture ( $\text{YP@SPB}$ ) was prepared using a mechanical mixing method with a weight ratio of  $8:2$ . Carbon powder was dispersed in 1-Methyl-2-pyrrolidinone (Sigma Aldrich, 99%) solvent and subsequently mixed with a polyvinylidene fluoride (PVDF, Solvay Corp)-based polymeric binder at an  $8:2$  weight ratio. The resulting Carbon@PVDF slurry was cast onto a polyethylene membrane (W-Scope, pore volume:  $43\%$ , pore size:  $60 \text{ nm}$ , thickness:  $16 \mu\text{m}$ ) with a film thickness of approximately  $30 \mu\text{m}$ . The coated membrane was then vacuum dried at  $50^\circ\text{C}$  for  $16 \text{ h}$ . The completed carbon-coated separator was punched into  $19 \text{ mm}$  diameter discs for further use.

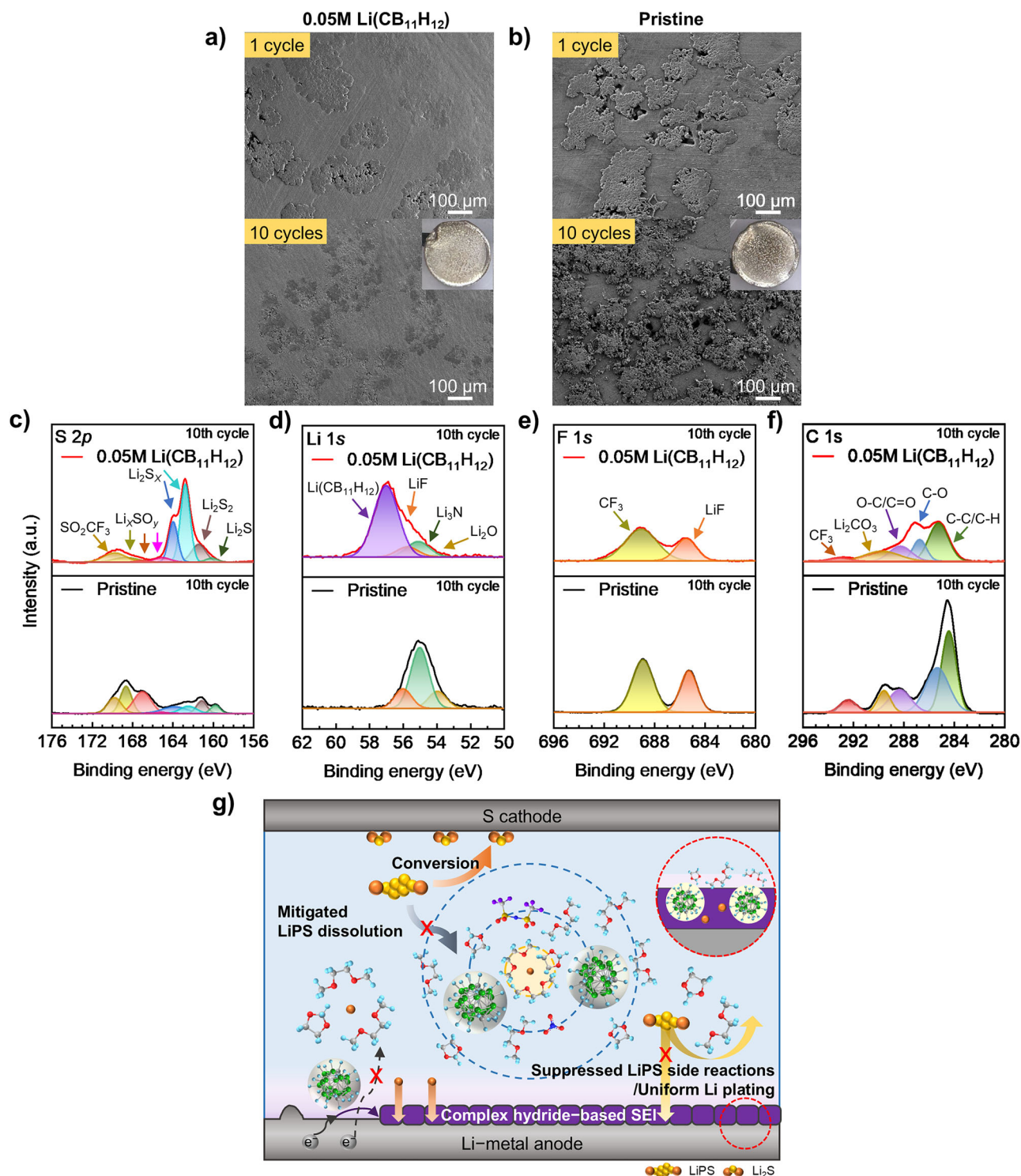


**Fig. 4 | Structural characterizations of the Li metal anodes during cycling.** SEM images of the Li metal anodes after 1 and 10 cycles at 0.1 C: **a** the 0.05 M Li(CB<sub>11</sub>H<sub>12</sub>) and **b** pristine electrolytes. Scale bars, 100  $\mu$ m. XPS spectra of **c** S 2p, **d** Li 1s, **e** F 1s,

and **f** C 1s of the Li metal anodes after 10 cycles. **g** Schematic illustration of the roles of the Li(CB<sub>11</sub>H<sub>12</sub>) additive in Li-S batteries.

### Preparation of electrolyte

The pristine electrolyte was fabricated by dissolving 1 M lithium bis(trifluoromethanesulfonyl)imide (LiTFSI, Sigma Aldrich, 99.95%) and 1.0 wt.% lithium nitrate (LiNO<sub>3</sub>, Sigma Aldrich, 99.99%) in 1,3-dioxolane (DOL, Sigma Aldrich, 99.95%) and 1,2-dimethoxyethane (DME, Sigma Aldrich, 99.5%) (1:1, volume ratio). The LiTFSI and LiNO<sub>3</sub> were dried under vacuum at 80 °C for 12 h prior to use. The Li(CB<sub>11</sub>H<sub>12</sub>) was obtained by drying the hydrated compounds under vacuum ( $<5 \times 10^{-2}$  Pa);

Li(CB<sub>11</sub>H<sub>12</sub>)·xH<sub>2</sub>O (Katchem) at 160 °C for 12 h. For comparison, various amounts of Li(CB<sub>11</sub>H<sub>12</sub>) were added to the pristine electrolyte. The Li(CB<sub>11</sub>H<sub>12</sub>) concentrations were adjusted to 0.05, 0.1, 0.3, and 0.5 M. These electrolytes were stirred for 12 h in a glove box filled with argon gas.

### Electrochemical measurements

All CR2032 coin cells (Wellcos Co.) were assembled in an argon-filled glove box (O<sub>2</sub> < 1 ppm and H<sub>2</sub>O < 1 ppm). A polyethylene membrane was used as



the separator. The Li–S full cell tests were performed in a two-electrode configuration with a carbon-coated separator, using lithium foil (Honjo, thickness of 100  $\mu\text{m}$ ). The Li–S full cells were filled with 25, 50, and 70  $\mu\text{L}$  of electrolyte. To evaluate electrochemical performance, a battery cycler (WBCS 3000, WonAtech) was used for galvanostatic discharge-charge measurements. The tests were cycled at 0.1 C (1 C = 1672  $\text{mA g}^{-1}$ ) and 25  $^{\circ}\text{C}$  from 1.8 to 2.8 V (vs.  $\text{Li}^{+}/\text{Li}$ ). For the rate performance evaluation, various currents ranging from 0.1 C to 2 C were used to measure the rate performance in the potential range of 1.8–2.8 V (vs.  $\text{Li}^{+}/\text{Li}$ ). To study the Li stripping/plating process, the  $\text{Li}|\text{Li}|$  symmetric cells were conducted at current densities of 0.5, 1.0, and 2.0  $\text{mA cm}^{-2}$ . The symmetric cells were filled with 70  $\mu\text{L}$  of electrolyte using a lithium foil (Honjo, thickness of 200  $\mu\text{m}$ ). After assembly, all the cells were kept at 25  $^{\circ}\text{C}$  for 12 h to allow electrolyte penetration. The cyclic voltammetry (CV) measurements were performed in the potential range of 1.8–2.8 V (vs.  $\text{Li}^{+}/\text{Li}$ ) for full cells at a scanning rate of 0.1  $\text{mV s}^{-1}$ . All electrochemical measurements were conducted in a 25  $^{\circ}\text{C}$  thermostatic chamber.

### Material characterization

The phase of the  $\text{Li}(\text{CB}_{11}\text{H}_{12})$  was performed with XRD (SmartLab, Rigaku) measurements with  $\text{Cu}_{K\alpha}$  radiation (wavelength  $\lambda = 1.5406 \text{ \AA}$  for  $K_{\alpha 1}$  and  $1.5444 \text{ \AA}$  for  $K_{\alpha 2}$ ) in the  $2\theta$  range of  $5^{\circ}$ – $50^{\circ}$ . For the powder XRD measurement, the sample was loaded into a thin-walled glass capillary under an Ar atmosphere and sealed with paraffin liquid. The bonding states of the electrolytes were characterized using Raman spectroscopy (LabRAM HR Evolution, Horiba). Nuclear Magnetic Resonance spectroscopy (NMR, JEOL–400 MHz spectrometer) was performed to confirm the enhanced coordination of  $\text{Li}^{+}$  by solvent molecules. NMR measurements were conducted in a coaxial NMR tube to avoid mixing with  $\text{D}_2\text{O}$ <sup>81</sup>. The dissolution behavior of  $\text{Li}_2\text{S}_6$  in DOL:DME was analyzed using UV-visible-near infrared (UV-Vis-NIR) absorption spectroscopy with a LAMBDA 950 spectrophotometer (PerkinElmer). Electrochemical impedance spectroscopy (EIS) measurements were performed in the 1 MHz–10 mHz frequency range at a voltage amplitude of 10 mV using a potentiostat (SP-300, Biologic). All electrochemical measurements were conducted in a 25  $^{\circ}\text{C}$  thermostatic chamber. The morphology and microstructure of the samples were examined using field-emission scanning electron microscopy (FE-SEM, GEMINI500, ZEISS) operated at 2 kV. The surface elemental composition of the S cathodes and the Li metal anodes before and after the plating process was confirmed using X-ray photoelectron spectroscopy (XPS). XPS measurements were performed using a Nexsa system (ThermoFisher Scientific) with a 100  $\mu\text{m}$  X-ray spot size.

### Data availability

The data that support the findings of this study are available from the corresponding authors upon reasonable request.

Received: 10 March 2025; Accepted: 28 August 2025;

Published online: 02 October 2025

### References

- Dunn, B., Kamath, H. & Tarascon, J. M. Electrical energy storage for the grid: a battery of choices. *Science* **334**, 928–935 (2011).
- Nitta, N., Wu, F., Lee, J. T. & Yushin, G. Li-ion battery materials: present and future. *Mater. Today* **18**, 252–264 (2015).
- Bruce, P. G., Freunberger, S. A., Hardwick, L. J. & Tarascon, J. M. Li– $\text{O}_2$  and Li–S batteries with high energy storage. *Nat. Mater.* **11**, 19–29 (2012).
- Manthiram, A., Fu, Y. & Su, Y. S. Challenges and prospects of lithium–sulfur batteries. *Acc. Chem. Res.* **46**, 1125–1134 (2013).
- Heo, J. et al. Advanced performance through mechanofusion-induced uniform interfacial layers for all-solid-state lithium–sulfur batteries. *Appl. Surf. Sci.* **688**, 162292 (2025).
- Xu, W. et al. Lithium metal anodes for rechargeable batteries. *Energy Environ. Sci.* **7**, 513–537 (2014).
- Ji, X. & Nazar, L. F. Advances in Li–S batteries. *J. Mater. Chem.* **20**, 9821–9826 (2010).
- Yin, Y. X., Xin, S., Guo, Y. G. & Wan, L. J. Lithium–sulfur batteries: electrochemistry, materials, and prospects. *Angew. Chem. Int. Ed.* **52**, 13186–13200 (2013).
- Heo, J. et al. Recent advances in achieving high energy/power density of lithium–sulfur batteries for current and near-future applications. *Battery Energy* **4**, e20240051 (2025).
- Barchasz, C. et al. Lithium/sulfur cell discharge mechanism: an original approach for intermediate species identification. *Anal. Chem.* **84**, 3973–3980 (2012).
- Rauh, R., Shuker, F., Marston, J. & Brummer, S. Formation of lithium polysulfides in aprotic media. *J. Inorg. Nucl. Chem.* **39**, 1761–1766 (1977).
- Mikhaylik, Y. V. & Akridge, J. R. Polysulfide shuttle study in the Li/S battery system. *J. Electrochem. Soc.* **151**, A1969 (2004).
- Yamin, H. et al. Lithium sulfur battery: oxidation/reduction mechanisms of polysulfides in THF solutions. *J. Electrochem. Soc.* **135**, 1045 (1988).
- Qian, J. et al. High rate and stable cycling of lithium metal anode. *Nat. Commun.* **6**, 6362 (2015).
- Tikekar, M. D., Choudhury, S., Tu, Z. & Archer, L. A. Design principles for electrolytes and interfaces for stable lithium-metal batteries. *Nat. Energy* **1**, 16114 (2016).
- Heo, J. et al. A promising approach to ultra-flexible 1 Ah lithium–sulfur batteries using oxygen-functionalized single-walled carbon nanotubes. *Adv. Sci.* **12**, 2406536 (2025).
- Aurbach, D. et al. On the surface chemical aspects of very high energy density, rechargeable Li–sulfur batteries. *J. Electrochem. Soc.* **156**, A694 (2009).
- Zhang, S. S. Role of  $\text{LiNO}_3$  in rechargeable lithium/sulfur battery. *Electrochim. Acta* **70**, 344–348 (2012).
- Mikhaylik, Y. V. Electrolytes for lithium sulfur cells. *United States Patent* US20080187840A1 (2008).
- Kim, J. S. et al. Poreless separator and electrolyte additive for lithium–sulfur batteries with high areal energy densities. *ChemNanoMat* **1**, 240–245 (2015).
- Jia, W. et al. Extremely accessible potassium nitrate ( $\text{KNO}_3$ ) as the highly efficient electrolyte additive in lithium battery. *ACS Appl. Mater. Interfaces* **8**, 15399–15405 (2016).
- Li, J. et al.  $\text{ZrO}(\text{NO}_3)_2$  as a functional additive to suppress the diffusion of polysulfides in lithium–sulfur batteries. *J. Power Sources* **442**, 227232 (2019).
- Liu, S., Li, G. R. & Gao, X. P. Lanthanum nitrate as electrolyte additive to stabilize the surface morphology of lithium anode for lithium–sulfur battery. *ACS Appl. Mater. Interfaces* **8**, 7783–7789 (2016).
- Wahyudi, W. et al. Lithium-ion desolvation induced by nitrate additives reveals new insights into high performance lithium batteries. *Adv. Funct. Mater.* **31**, 2101593 (2021).
- Li, S. et al. Designing Li-protective layer via  $\text{SOCl}_2$  additive for stabilizing lithium–sulfur battery. *Energy Storage Mater.* **18**, 222–228 (2019).
- Li, J. et al. Potassium hexafluorophosphate additive enables stable lithium–sulfur batteries. *ACS Appl. Mater. Interfaces* **12**, 56017–56026 (2020).
- Hu, T. et al. Uniform lithium deposition induced by copper phthalocyanine additive for durable lithium anode in lithium–sulfur batteries. *Chin. Chem. Lett.* **35**, 108603 (2024).
- Unemoto, A., Matsuo, M. & Orimo, S. I. Complex hydrides for electrochemical energy storage. *Adv. Funct. Mater.* **24**, 2267–2279 (2014).
- Matsuo, M. & Orimo, S. I. Lithium fast-ionic conduction in complex hydrides: review and prospects. *Adv. Energy Mater.* **1**, 161–172 (2011).
- Matsuo, M. et al. Lithium superionic conduction in lithium borohydride accompanied by structural transition. *Appl. Phys. Lett.* **91**, 224103 (2007).



31. Teprovich, J. A. et al. Bi-functional  $\text{Li}_2\text{B}_{12}\text{H}_{12}$  for energy storage and conversion applications: solid-state electrolyte and luminescent down-conversion dye. *J. Mater. Chem. A* **3**, 22853–22859 (2015).
32. Tang, W. S. et al. Unparalleled lithium and sodium superionic conduction in solid electrolytes with large monovalent cage-like anions. *Energy Environ. Sci.* **8**, 3637–3645 (2015).
33. Toyama, N. et al. Lithium ion conductivity of complex hydrides incorporating multiple closo-type complex anions. *J. Energy Chem.* **38**, 84–87 (2019).
34. Tang, W. S. et al. Liquid-like ionic conduction in solid lithium and sodium monocarba-closo-decaborates near or at room temperature. *Adv. Energy Mater.* **6**, 1502237 (2016).
35. Mohtadi, R. & Orimo, S. I. The renaissance of hydrides as energy materials. *Nat. Rev. Mater.* **2**, 1–15 (2016).
36. Dorai, A. et al. Understanding ion dynamics in closoborate-type lithium-ion conductors on different time-scales. *J. Phys. Chem. Lett.* **15**, 4864–4871 (2024).
37. Kisu, K. et al. Fast divalent conduction in  $\text{MB}_{12}\text{H}_{12} \cdot 12\text{H}_2\text{O}$  (M = Zn, Mg) complex hydrides: effects of rapid crystal water exchange and application for solid-state electrolytes. *J. Mater. Chem. A* **10**, 24877–24887 (2022).
38. Yang, F. et al. A dynamic database of solid-state electrolyte (DDSE) picturing all-solid-state batteries. *Nano Mater. Sci.* **6**, 256–262 (2024).
39. Kim, T., Lee, T. & Kim, S. Synthesis and electrochemical properties of hydrosulfide solid electrolytes. *Korean J. Chem. Eng.* 1–7 (2024).
40. Unemoto, A. et al. Development of bulk-type all-solid-state lithium-sulfur battery using  $\text{LiBH}_4$  electrolyte. *Appl. Phys. Lett.* **105**, 083901 (2014).
41. Kim, H., Park, K. & Kim, S. High sulfur content cathode composites utilizing the  $\text{Li}(\text{CB}_9\text{H}_{10})_{0.7}(\text{CB}_{11}\text{H}_{12})_{0.3}$  superionic conductor for all–solid–state Li–S batteries. *J. Power Sources* **621**, 235284 (2024).
42. Kim, S. et al. A complex hydride lithium superionic conductor for high-energy-density all-solid-state lithium metal batteries. *Nat. Commun.* **10**, 1081 (2019).
43. Kim, S., Kisu, K. & Orimo, S. I. Stabilization of superionic-conducting high-temperature phase of  $\text{Li}(\text{CB}_9\text{H}_{10})$  via solid solution formation with  $\text{Li}_2(\text{B}_{12}\text{H}_{12})$ . *Crystals* **11**, 330 (2021).
44. Kim, S. et al. Fast lithium-ion conduction in atom-deficient closo-type complex hydride solid electrolytes. *Chem. Mater.* **30**, 386–391 (2018).
45. Kim, S. et al. Room temperature operation of all-solid-state battery using a closo-type complex hydride solid electrolyte and a  $\text{LiCoO}_2$  cathode by interfacial modification. *J. Energy Chem.* **43**, 47–51 (2020).
46. Kim, H. et al. Aqueous synthesis of lithium superionic-conducting complex hydride solid electrolytes. *J. Mater. Chem. A* **12**, 32132–32139 (2024).
47. Lee, T. et al. Hydrogen-rich argyrodite solid electrolytes for NCM/Li all-solid-state batteries. *ACS Energy Lett.* **9**, 4493–4500 (2024).
48. Strauss, S. H. The search for larger and more weakly coordinating anions. *Chem. Rev.* **93**, 927–942 (1993).
49. Körbe, S., Schreiber, P. J. & Michl, J. Chemistry of the Carba-closo-dodecaborate (–) Anion,  $\text{CB}_{11}\text{H}_{12}$ . *Chem. Rev.* **106**, 5208–5249 (2006).
50. Seo, D. M. et al. Electrolyte solvation and ionic association II. Acetonitrile-lithium salt mixtures: highly dissociated salts. *J. Electrochem. Soc.* **159**, A1489 (2012).
51. Herstedt, M. et al. Spectroscopic characterization of the conformational states of the bis(trifluoromethanesulfonyl) imide anion ( $\text{TFSI}^-$ ). *J. Raman Spectrosc.* **36**, 762–770 (2005).
52. Yoshida, H. & Matsuura, H. Density functional study of the conformations and vibrations of 1,2-dimethoxyethane. *J. Phys. Chem. A* **102**, 2691–2699 (1998).
53. Tretyakov, D. O. et al. Formation of contact ion pairs and solvation of  $\text{Li}^+$  ion in sulfones: Phase diagrams, conductivity, Raman spectra, and dynamics. *J. Chem. Eng. Data* **55**, 1958–1964 (2010).
54. Skripov, A. V. et al. Anion reorientations and cation diffusion in  $\text{LiCB}_{11}\text{H}_{12}$  and  $\text{NaCB}_{11}\text{H}_{12}$ :  $^1\text{H}$ ,  $^7\text{Li}$ , and  $^{23}\text{Na}$  NMR studies. *J. Phys. Chem. C* **119**, 26912–26918 (2015).
55. Kim, S. et al. Complex hydride solid electrolytes of the  $\text{Li}(\text{CB}_9\text{H}_{10})$ – $\text{Li}(\text{CB}_{11}\text{H}_{12})$  quasi-binary system: relationship between the solid solution and phase transition, and the electrochemical properties. *ACS Appl. Energy Mater.* **3**, 4831–4839 (2020).
56. Wan, C. et al. Natural abundance  $^{17}\text{O}$ ,  $^6\text{Li}$  NMR and molecular modeling studies of the solvation structures of lithium bis (fluorosulfonyl) imide/1, 2-dimethoxyethane liquid electrolytes. *J. Power Sources* **307**, 231–243 (2016).
57. Gerathanassis, I. P. Oxygen-17 NMR spectroscopy: basic principles and applications (Part I). *Prog. Nucl. Magn. Reson. Spectrosc.* **56**, 95–197 (2010).
58. Kisu, K. et al. Enhanced durability of a metal battery with dual salt: synergistic effect on solid electrolyte interphase and solvation structure for improved electrodeposition. *ACS Appl. Mater. Interfaces* **17**, 1322–1331 (2024).
59. Belkova, N. V., Epstein, L. M., Filippov, O. A. & Shubina, E. S. Hydrogen and dihydrogen bonds in the reactions of metal hydrides. *Chem. Rev.* **116**, 8545–8587 (2016).
60. Su, C.-C. et al. Internally referenced DOSY-NMR: a novel analytical method in revealing the solution structure of lithium-ion battery electrolytes. *J. Phys. Chem. Lett.* **9**, 3714–3719 (2018).
61. Li, D., Keresztes, I., Hopson, R. & Williard, P. G. Characterization of reactive intermediates by multinuclear diffusion-ordered NMR spectroscopy (DOSY). *Acc. Chem. Res.* **42**, 270–280 (2009).
62. Tang, W. S. et al. Stabilizing superionic-conducting structures via mixed-anion solid solutions of monocarba-closo-borate salts. *ACS Energy Lett.* **1**, 659–664 (2016).
63. Zhang, S. S. Liquid electrolyte lithium/sulfur battery: fundamental chemistry, problems, and solutions. *J. Power Sources* **231**, 153–162 (2013).
64. Kim, S. C. et al. Solvation-property relationship of lithium-sulphur battery electrolytes. *Nat. Commun.* **15**, 1268 (2024).
65. Kim, S. C. et al. Potentiometric measurement to probe solvation energy and its correlation to lithium battery cyclability. *J. Am. Chem. Soc.* **143**, 10301–10308 (2021).
66. Suo, L. et al. A new class of solvent-in-salt electrolyte for high-energy rechargeable metallic lithium batteries. *Nat. Commun.* **4**, 1481 (2013).
67. Huang, F. et al. Akin solid–solid biphasic conversion of a Li–S battery achieved by coordinated carbonate electrolytes. *J. Mater. Chem. A* **7**, 12498–12506 (2019).
68. Unemoto, A. et al. Stable interface formation between  $\text{TiS}_2$  and  $\text{LiBH}_4$  in bulk-type all-solid-state lithium batteries. *Chem. Mater.* **27**, 5407–5416 (2015).
69. Diao, Y., Xie, K., Xiong, S. & Hong, X. Insights into Li-S battery cathode capacity fading mechanisms: irreversible oxidation of active mass during cycling. *J. Electrochem. Soc.* **159**, A1816 (2012).
70. Hendrickson, D. N., Hollander, J. M. & Jolly, W. L. Core-electron binding energies for compounds of boron, carbon, and chromium. *Inorg. Chem.* **9**, 612–615 (1970).
71. Ota, H. et al. Characterization of Lithium electrode in lithium imides/ethylene carbonate and cyclic ether electrolytes: II. Surface chemistry. *J. Electrochem. Soc.* **151**, A437 (2004).
72. Xiong, S., Xie, K., Diao, Y. & Hong, X. Properties of surface film on lithium anode with  $\text{LiNO}_3$  as lithium salt in electrolyte solution for lithium–sulfur batteries. *Electrochim. Acta* **83**, 78–86 (2012).
73. Wu, H.-L. et al. Thiol-based electrolyte additives for high-performance lithium-sulfur batteries. *Nano Energy* **32**, 50–58 (2017).
74. Wei, J. Y. et al. Shielding polysulfide intermediates by an organosulfur-containing solid electrolyte interphase on the lithium anode in lithium–sulfur batteries. *Adv. Mater.* **32**, 2003012 (2020).

75. Kim, S., Kwon, Y. M., Cho, K. Y. & Yoon, S. Metal iodides ( $\text{LiI}$ ,  $\text{MgI}_2$ ,  $\text{AlI}_3$ ,  $\text{TiI}_4$ , and  $\text{SnI}_4$ ) potentiality as electrolyte additives for Li–S batteries. *Electrochim. Acta* **391**, 138927 (2021).
76. Park, J.-W. et al. Ionic liquid electrolytes for lithium–sulfur batteries. *J. Phys. Chem. C* **117**, 20531–20541 (2013).
77. Wu, M.-X. et al. Improving the uniformity of lithium deposition via ionic liquid additives for long-cycling lithium–sulfur batteries. *Chin. Chem. Lett.* **368**, 111330 (2025).
78. Lu, H. et al. A hybrid ionic liquid-based electrolyte for high-performance lithium–sulfur batteries. *N. J. Chem.* **44**, 361–368 (2020).
79. Zheng, J. et al. Ionic liquid-enhanced solid state electrolyte interface (SEI) for lithium–sulfur batteries. *J. Mater. Chem. A* **1**, 8464–8470 (2013).
80. Jiang, Y. et al. Multi-effect ionic liquid additives achieve high cycle stability lithium-sulfur batteries by constructing an electrostatic shielding layer and eliminating ‘dead sulfur’. *Adv. Funct. Mater.* **35**, 2500077 (2025).
81. Wahyudi, W. et al. Hitherto unknown solvent and anion pairs in solvation structures reveal new insights into high-performance lithium-ion batteries. *Adv. Sci.* **9**, 2202405 (2022).

## Acknowledgements

This work is supported by the National Research Foundation of Korea (NRF) grant funded by the Ministry of Science and ICT (MSIT) (No. RS-2023-00252931), the Commercialization Promotion Agency for R&D Outcomes (COMPA) grant funded by the Korea government (Ministry of Science and ICT) (No. RS-2025-02316415), the Korea Institute for Advancement of Technology (KIAT) grant funded by the Ministry of Trade, Industry and Energy (MOTIE) (No. 00432185), Seoul R&BD Program (HM240027), the Industrial Technology Innovation Program (Next-generation High-Energy-Density Lithium Sulfur Battery Development) of the Ministry of Trade, Industry and Energy of the Republic of Korea (P268600148), and the National Research Council of Science & Technology (NST) grant by the Korea government (MSIT) (No. GTL24012-000). The authors also acknowledge the GIST Advanced Institute of Instrumental Analysis (GAIA) for providing access to the instrumental facilities, including the [SS05] Raman system, the [SP02] M-XRD system, and the [SS06] UV–VIS–NIR Spectrophotometer.

## Author contributions

So.K.: led the investigation, data curation, formal analysis, and methodology development; designed and conducted the experiments; drafted the original manuscript; and produced the visualizations. J.H.: contributed to the investigation and experimental design, conducted the experiments, and provided writing review and editing of the manuscript. H.G.: assisted in the investigation and experimental procedures and contributed to data

acquisition. H.O., T.L.: provided writing review and editing of the manuscript. Y.L.: assisted with NMR measurements and contributed to data acquisition. K.K., S.O.: provided resources and performed sample preparation. J.P., S.K.: contributed to conceptualization, resources, supervision, writing review, manuscript editing, project administration, funding acquisition, overall project direction, and final approval.

## Competing interests

The authors declare no competing interests.

## Additional information

**Supplementary information** The online version contains supplementary material available at <https://doi.org/10.1038/s43246-025-00932-x>.

**Correspondence** and requests for materials should be addressed to Jun-Woo Park or Sangryun Kim.

**Peer review information** *Communications Materials* thanks the anonymous reviewers for their contribution to the peer review of this work. [A peer review file is available].

**Reprints and permissions information** is available at <http://www.nature.com/reprints>

**Publisher's note** Springer Nature remains neutral with regard to jurisdictional claims in published maps and institutional affiliations.

**Open Access** This article is licensed under a Creative Commons Attribution-NonCommercial-NoDerivatives 4.0 International License, which permits any non-commercial use, sharing, distribution and reproduction in any medium or format, as long as you give appropriate credit to the original author(s) and the source, provide a link to the Creative Commons licence, and indicate if you modified the licensed material. You do not have permission under this licence to share adapted material derived from this article or parts of it. The images or other third party material in this article are included in the article's Creative Commons licence, unless indicated otherwise in a credit line to the material. If material is not included in the article's Creative Commons licence and your intended use is not permitted by statutory regulation or exceeds the permitted use, you will need to obtain permission directly from the copyright holder. To view a copy of this licence, visit <http://creativecommons.org/licenses/by-nc-nd/4.0/>.

© The Author(s) 2025